International Journal of Applied Earth Observation and Geoinformation 122 (2023) 103388

Contents lists available at ScienceDirect

International Journal of Applied Earth Observation and Geoinformation

journal homepage: www.elsevier.com/locate/jag

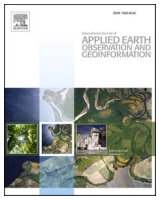

Monitoring the Mauna Loa (Hawaii) eruption of November–December 2022 from space: Results from GOES-R, Sentinel-2 and Landsat-8/9 observations

Nicola Genzano [a,c], Francesco Marchese [b,c,*], Simon Plank [d], Nicola Pergola [b,c]

[a] School of Engineering, University of Basilicata, Potenza, Italy
[b] Institute of Methodologies for Environmental Analysis, National Research Council, Tito Scalo (Pz), Italy
[c] Satellite Application Centre (SAC), Space Technologies and Applications Centre (STAC), Potenza, Italy
[d] German Remote Sensing Data Center, German Aerospace Center (DLR), Oberpfaffenhofen, Germany

ARTICLE INFO

Keywords:
Mauna Loa
GOES-R
Sentinel-2
Landsat-8/9
Normalised Hotspot Indices

ABSTRACT

Mauna Loa, one of the most actives volcanoes on Earth, is a shield volcano, located on the Island of Hawaii (USA). On 27 November 2022, after about 38 years of quiescence, a new eruptive activity took place at the Moku'āweoweo caldera, continuing in the following days (i.e. until 10 December) from the fissure vents opening on the Northeast Rift Zone. In this work, we investigate the Mauna Loa November – December 2022 eruption from space, integrating the information from different satellite sensors. The analysis of short-wave infrared (SWIR) data, at 10 min temporal resolution, from the Advanced Baseline Imager (ABI), aboard the Geostationary Operational Environmental Satellites – R series (GOES-R), performed through the Normalised Hotspot Indices (NHI), indicates that the Mauna Loa eruption started on 27 November in between 23:10–23:20 LT (28 November at 09:10–09:20 UTC). The same analysis shows the increase of thermal activity and its progressive reduction from the early morning of 28 November, in agreement with the eruption migration from the summit caldera to the Northeast Rift Zone. By analysing the second phase of eruption through SWIR data from the Multispectral Instrument (MSI) and Operational Land Imager (OLI), respectively aboard Sentinel-2 and Landsat 8/9 satellites, we estimated a maximum lava flow length of 17 km. Moreover, we retrieved values of the volcanic radiative power (VRP) up to 65 GW, and a time-averaged discharge rate (TADR) of ~1000 (±500) m^3/s. These results show that SWIR observations, at different spatial and temporal resolution, may give an important contribution to the monitoring, mapping and characterisation of intense lava effusions.

1. Introduction

Several research studies demonstrated the important role of satellite observations in the monitoring of thermal volcanic activity. MIR (medium infrared; 3–5 μm) and TIR (thermal infrared; 8–14 μm) data, at 1 km spatial resolution, from AVHRR (Advanced Very High Resolution Radiometer) and MODIS (Moderate Resolution Imaging Spectroradiometer), were largely used to detect volcanic thermal features (e.g., Higgins & Harris, 1997; Coppola et al., 2016; Coppola et al., 2020; Pergola et al., 2004; Wright et al., 2002, Wright & Pilger 2008). Those data were analysed also to investigate the pre-eruptive thermal phases of active volcanoes (e.g., Pergola et al., 2004; Marchese et al., 2012; Girona et al., 2021), and retrieve quantitative information about thermal anomalies (e.g., Coppola et al., 2013; Piscini & Lombardo 2014; Wright & Pilger 2008; Wright et al., 2015). Indeed, starting from the dual band method (Dozier, 1981), some improved versions of this technique (e.g., three thermal component pixel model; Harris et al., 1999) were used for better characterising the subpixel hotspots (for temperature and size), before estimating the radiative power. This parameter was largely retrieved, from night-time MODIS data, through the MIR band approach (Wooster et al., 2003).

This method is used operationally also by FIRMS (Fire Information for Resource Management System; https://firms.modaps.eosdis.nasa.gov/), providing hotspot products at global scale, through the analysis of MODIS and VIIRS (Visible Infrared Imaging Radiometer Suite) data at 375 m and 750 m spatial resolution. Estimates of volcanic radiative power (VRP) were then used to derive the time-averaged discharge rate (TADR), i.e., the lava volume flux averaged over a given time period (e.g., Harris et al. 2007), which is a critical parameter for numerical models simulating the lava flow paths (e.g., Ganci et al., 2012; Ganci et al.,

* Corresponding author.
E-mail address: francesco.marchese@cnr.it (F. Marchese).

https://doi.org/10.1016/j.jag.2023.103388
Received 20 February 2023; Received in revised form 5 June 2023; Accepted 9 June 2023
Available online 15 June 2023

2020).

Among the studies investigating volcanic thermal anomalies from space, some of them were focused on Kilauea (Hawaii, USA), showing frequent and large eruptions (e.g., Harris et al., 2001; 2007; Murphy et al., 2013; Marchese et al., 2022; Musacchio et al., 2023; Plank et al., 2021). Those studies were performed also using SWIR (shortwave infrared; 1.5–3 μm) data from MSI (Multispectral Imager) and OLI (Operational Land Imager), respectively aboard Sentinel-2 and Landsat 8 satellites, which are sensitive to the hot targets (e.g., Murphy et al., 2016; Marchese et al., 2018; 2019; Gray et al., 2019).

In this work, we integrate SWIR observations from MSI, OLI/OLI-2 and ABI (Advanced Baseline Imager) aboard the GOES-R (Geostationary Operational Environmental Satellites-R) satellites, to investigate another active Hawaiian volcano. We analyse the November – December 2022 eruption of Mauna Loa, which started at the summit caldera in the late evening of 27 November, after about 38 years of quiescence, and continued until 10 December, from fissure vents opening on the Northeast Rift Zone at a high elevation (Global Volcanism Program, 2022a; Global Volcanism Program, 2022b).

While SWIR data at high temporal resolution (10 min) from ABI are used here to investigate the eruption onset, those at higher spatial resolution (up to 20 m) from MSI and OLI/OLI2 are analysed to characterise the active lava flows in terms of VRP and TADR. A first comparison with the previous 1984 eruption is then performed.

2. Mauna Loa and the November-December 2022 eruption chronology

Mauna Loa Volcano is located on the Big Island of Hawai'i (USA); by covering an area of about 5,100 km^2, it is the largest active volcano on Earth (Miklius & Cervelli, 2003).

The summit area, above 3,660 m elevation, includes the Moku'āweoweo caldera and the upper-most parts of the two rift zones (U.S. Geological Survey, 2022a). Since 1843, when pāhoehoe flows of exceptional length were produced, Mauna Loa has erupted 33 times, with time intervals ranging from months to decades (Riker et al., 2009).

On 25 March 1984, an effusive eruption, revealed by a military satellite, took place at the summit caldera (Lockwood et al., 1985). The eruption migrated, a few hours later, to the Northeast Rift Zone, feeding a lava flow extending to about 5 km down the southeast flank (U.S. Geological Survey 2022b). In the afternoon of the same day, some eruptive vents opened in between 2,800–2,900 m elevation, becoming the source of the lava flows during the following phase of eruption (Lipman et al., 1985; Lipman & Banks, 1987). The latter had a time duration of about 3 weeks and was characterised by lava flows extending up to 27 km from the eruptive vents (Lockwood et al., 1985; Lipman & Banks 1987). In the months following the eruption, Mauna Loa showed some deep, long-period earthquake swarms, while in between 2004 and 2010, the Hawaiian Volcano Observatory (HVO) of USGS reported some variations in the gas emissions. The analysis of InSAR (Interferometric Synthetic Aperture Radar) data provided information about the intrusive bodies causing surface deformation (Amelung et al., 2007; Global Volcanism Program, 2012). Since mid-September 2022, a new state of heightened unrest occurred, with the increase in the earthquake activity and the inflation of the summit (U.S. Geological Survey, 2022c).

On 27 November, a new eruption started at the summit caldera at around 23:30 LT (UTC-10) (U.S. Geological Survey 2022c). Lava flows were initially contained within the summit area, and visible from the Kona district. The day after the eruption migrated from the summit to the Northeast Rift Zone, where the fissures fed several lava flows. An overflight from HVO, performed on 28 November around 06:30 LT, revealed the presence of three fissures at high elevation, which were the source of the lava flows travelling towards Northern and North-eastern directions (U.S. Geological Survey, 2022c). Lava fountains along the fissures also occurred, while the sulphur dioxide (SO_2) emission rates were estimated around 250,000 tons per day (t/d). On 29 November, the main lava flow was issued from fissure 3 (Fig. 1), where the fountains were 40–50 m tall.

A lava fountain activity was recorded also at fissure 4, which probably formed the day before at around 19:30 LT. The Moku'āweoweo caldera was inactive, and there was no lava erupting from the Southwest Rift Zone (U.S. Geological Survey, 2022d). On 30 November, two active fissures feed the lava flows. Those from fissure 3 moved to the north toward the Highway (Saddle Road), while the largest flow slowed in the evening of the same day. Lava flows from fissure 4 moved towards the northeast direction (U.S. Geological Survey, 2022e). On 1 December 2022, lava flow advanced at an average rate of 45 m per hour, and the SO_2 emission rates were around 180,000 t/d. The day after the main flow front was 4.3 km from the Saddle Road; fissure 4, although active, showed a less intense eruptive activity (U.S. Geological Survey, 2022f). On 3 December, the lava flow from fissure 3 advanced at an average rate of about 13 m per hour, while the fissure 4 was no longer active (U.S. Geological Survey, 2022g). The day after, the flow front was about 2.6 km from the Saddle Road; on 5 December, fissure 3 was feeding the lava flow with an average rate of 6 m per hour (U.S. Geological Survey, 2022h). On 6 December, the lava flow was inactive for most of its lower length. Two days later, lava continued to be emitted only from fissure 3, although with a reduced rate (U.S. Geological Survey, 2022i).

On 10 December, lava supply on the Northeast Rift Zone ceased, and SO_2 emissions decreased to the near pre-eruption background levels (U.S. Geological Survey, 2022l). The lava flows extended up to about 19 km from the active vents, in the north/northeast direction, before the eruption ending (U.S. Geological Survey, 2022m).

3. Data and methods

3.1. GOES-R ABI data

Geostationary satellite sensors, by providing infrared data with a higher temporal resolution than the polar-orbiting ones, enable a frequent and more continuous monitoring of thermal volcanic activity (e.g., Mouginis-Mark et al., 2000; Harris et al., 2001; Pergola et al., 2008; Calvari et al., 2021; Thompson et al., 2022).

ABI is the primary instrument of the GOES-R satellites, a four-satellite program designed to observe the Western hemisphere, from the National Oceanic and Atmospheric Administration (NOAA), supported by the National Aeronautics and Space Administration (NASA). This instrument delivers visible to infrared data every 10 min, in 16 different spectral bands. Table 1 details the spectral bands commonly

Fig. 1. Aerial photograph of November 29, 2022, at around 08:00 LT of the fissure 3, erupting on the Northeast Rift Zone of Mauna Loa (Hawaii, USA). Credits: USGS-Photo by M. Patrick.

Table 1
ABI bands commonly used to detect and monitor volcanic thermal features.

ABI band	Wavelength Range (μm)	Spatial Resolution (km)
Band 5 (SWIR1)	1.58–1.64	1
Band 6 (SWIR2)	2.22–2.27	2
Band 7 (MIR)	3.80–4.00	2
Band 13 (TIR)	10.1–10.6	2
Band 14 (TIR)	10.8–11.6	2

used to detect and monitor volcanic thermal features.

In this work, we use the GOES-17 ABI data, covering the Hawaii Islands, the west part of North America and a portion of the Pacific Ocean (e.g., Gunshor et al., 2020; Zhao & Ban, 2022), to investigate the Mauna Loa eruption onset. In particular, the Cloud and Moisture Imagery (CMI) products, generated both for reflective and emissive bands (at 2 km spatial resolution) and available in Google Earth Engine (GEE), were analysed for this purpose. GEE is a cloud-based platform for geospatial analyses, which offers an extended data catalogue of satellite observations together with massive computational capabilities (Gorelick et al., 2017). The imagery value of the CMI data is a dimensionless reflectance factor normalized by the solar zenith angle for bands 1–6, and the brightness temperature at the Top of the Atmosphere for bands 7–16 (Earth Engine Data Catalogue, 2022). We analysed more than 12,000 GOES-R ABI scenes, including night-time and daytime observations, through the GEE platform using the method described in section 3.3.

3.2. Sentinel-2 MSI and Landsat-8/9 OLI/OLI2 data

The OLI instrument, aboard the Landsat-8 satellite, having a 16-day repeat cycle with an equatorial crossing time of 10:00 a.m. +/- 15 min, provides data in nine spectral bands; the NIR and SWIR have a spatial resolution of 30 m (Table 2). The almost identical OLI2 sensor, aboard the Landsat-9 satellite, offers a higher dynamic range than OLI (14-bit vs 12-bit) (National Aeronautics & Space Administration 2022). The MSI instrument, aboard the Sentinel-2A/2B satellites (joint 5-day revisit time at the equator), delivers data in 13 spectral channels, with a higher spatial resolution than OLI/OLI2 in the NIR and SWIR bands (Table 2) (European Space Agency 2022).

Both OLI and MSI data were extensively used to localise and map hot targets (e.g., Gray et al., 2019; Kato et al. 2021; Marchese et al., 2018; Murphy et al., 2016; Plank et al., 2020; Wu et al., 2022), encouraging the development of some automated hotspot detection methods performing operationally (e.g., Marchese et al., 2019; Massimetti et al., 2020).

3.3. Normalised hotspots Indices (NHI)

The Normalised Hotspot Indices (NHI), proposed in Marchese et al., (2019), are defined as:

Table 2
OLI and MSI (S2A) bands used to map high-temperature features.

Sensor	Spectral Band	Wavelength Range (μm)	Spatial Resolution (m)
OLI/OLI2	B5 (NIR)	0.85–0.88	30
OLI/OLI2	B6 (SWIR1)	1.57–1.65	30
OLI/OLI2	B7 (SWIR2)	2.10–2.29	30
MSI (S2A)	B8A (NIR)	0.85–0.87	20
MSI (S2A)	B11 (SWIR1)	1.56–1.65	20
MSI (S2A)	B12 (SWIR2)	2.10–2.28	20

$$NHI_{SWIR} = \frac{L_{SWIR2} - L_{SWIR1}}{L_{SWIR2} + L_{SWIR1}} \quad (1)$$

$$NHI_{SWNIR} = \frac{L_{SWIR1} - L_{NIR}}{L_{SWIR1} + L_{NIR}} \quad (2)$$

Where L_{SWIR1} and L_{SWIR2} are the top of atmosphere (TOA) radiances measured in the SWIR bands of MSI/OLI, centred at 1.6 μm (SWIR1) and 2.2 μm (SWIR2) respectively, while L_{NIR} is the radiance measured in the NIR band at around 0.86 μm (Table 2).

The NHI behaviour was assessed by analysing hundreds of daytime Sentinel-2 MSI and Landsat-8 OLI scenes, acquired over different volcanic areas (Marchese et al., 2019). The study showed that the NHI_{SWIR} assumes positive values in presence of thermal anomalies from a low to a moderate intensity level (e.g., small lava overflows, high-temperature fumaroles) increasing the SWIR2 above the SWIR1 radiances. More intense thermal features (e.g., lava lakes, spatially extended lava flows) usually determine a more significant increment of the SWIR1 radiance, which coupled with a lower saturation radiance of the SWIR2 band of MSI/OLI, lead to negative values of the same index observed also over background and cloudy areas. On the contrary, the NHI_{SWNIR} assumes positive values mainly in presence of intense (for temperature and size) thermal anomalies, due to the increase of SWIR1 above the NIR radiance (Marchese et al., 2019; Genzano et al., 2020; Faruolo et al., 2022a; Faruolo et al., 2022b).

By combining the two indices, the NHI algorithm is capable of performing an efficient mapping of high-temperature features (e.g., Genzano et al., 2020)with some limitation, mainly including: *i)* a dependence on clouds and degassing plumes, which may partially or completely obscure the underlying hot targets; *ii)* the possible occurrence of missed detections in presence of weak thermal activities; *iii)* the underestimation of thermal anomalies in presence of extremely hot targets, causing the pixel saturation in both SWIR bands of MSI/OLI.

Moreover, false positives may occur in presence of vegetation fires occurring along the flanks/slopes of some volcanoes, and because of data issues (e.g., multispectral misregistration and striping of S2-MSI images). To minimize the false detections, we implemented an initial test on SWIR radiance and a spectral test for data issues within the interactive NHI tool (Genzano et al., 2020). The latter, also including an additional test for the extremely hot pixels, was developed under the GEE platform. The tool aim allows users to generate plots of the number of hot pixels, total SWIR radiance and hotspot area over the areas of interest (more than 1400 volcanoes listed by the Global Volcanism Program) with low processing times, after setting a distance buffer. Those products may be used also as input to change detection methods (Rösch & Plank, 2022; Orynbaikyzy et al., 2023).

The NHI performance were assessed in different areas including the Oldoynio Lengai (Tanzania) (Genzano et al., 2020), which is characterised by the emission of natrocarbonatite lava at relatively low temperatures (495–590 °C) (Vaughan et al. 2008). Moreover, by testing the automated module of the tool (NHI system) performing globally, we estimated a false positive rate around 15% during the first six months of operation. The study confirmed the NHI sensitivity to small high-temperature targets, as indicated for instance by the thermal anomaly flagged at Great Sitkin (Alaska, USA) a few days before the lava dome growth reported by the AVO (Alaska Volcano Observatory) (Marchese & Genzano, 2023). Thanks to those performance, and despite a certain delay of the data ingestion in GEE, the NHI tool/system may successfully integrate information from high temporal resolution satellite data.

Although the NHI algorithm was designed to perform on S2-MSI and L8-OLI data, it may provide information about hot targets even through satellite observations at coarse spatial resolution (Faruolo et al., 2022a). A negative threshold, tailored to those data, could then enable a more efficient identification of these features in daylight conditions (Falconieri et al., 2022).

In this work, we analyse the short-term variations of the NHI_{SWIR}

index, from the ABI CMI products, to retrieve information about the starting time of the Mauna Loa's eruption. The index was calculated from the formulation used to convert from the reflectance factor to radiance:

$$NHI_{SWIR} = \frac{L_{SWIR2} - L_{SWIR1}}{L_{SWIR2} + L_{SWIR1}} = \frac{\left(\frac{p_{f6}E_{sun6}}{\pi d^2} - \frac{p_{f5}E_{sun5}}{\pi d^2}\right)}{\left(\frac{p_{f6}E_{sun6}}{\pi d^2} + \frac{p_{f5}E_{sun5}}{\pi d^2}\right)} = \frac{\left(p_{f6}E_{sun6}\right) - \left(p_{f5}E_{sun5}\right)}{\pi d^2} \times \frac{\pi d^2}{\left(p_{f6}E_{sun6}\right) + \left(p_{f5}E_{sun5}\right)} = \frac{\left(p_{f6}E_{sun6}\right) - \left(p_{f5}E_{sun5}\right)}{\left(p_{f6}E_{sun6}\right) + \left(p_{f5}E_{sun5}\right)} \quad (3)$$

where, p_{f6} and p_{f5} are the reflectance factors in the CMI bands 5 (SWIR1) and 6 (SWIR2), E_{sun6} and E_{sun6} are the in-band solar irradiance at 1 Astronomical Unit (AU), and d the ratio of the actual distance to the mean Earth–sun distance (NOAA-NESDIS, 2012).

3.4. Radiative power and TADR estimations from MSI and OLI/OLI2 data

To estimate the radiative power Φ_{rad} [W] from daytime S2-MSI, L8-OLI and L9-OLI2 data, we used the following formulation:

$$\phi_{rad} = \varepsilon\sigma A(T_h^4 - T_b^4) \quad (4)$$

where σ is the Stefan–Boltzmann constant, (A) is the pixel area (e.g., 400 m^2 in case of S2-MSI data), T_h is the temperature of the hot pixel retrieved from the SWIR1 radiance corrected for the influence of the solar irradiation (see Marchese et al., 2022), and T_b is the temperature of the cold background. Information about this parameter were derived from weather stations according to the date and time of the satellite acquisitions. We assumed an emissivity $\varepsilon = 0.95$ in equation (4) (cf. Lombardo et al. (2020), who analysed in the SWIR range the emissivity of molten basalt at magmatic temperatures). The VRP per satellite acquisition was computed by summing up ϕ_{rad} over all hot pixels flagged by the NHI_{SWNIR} in each single satellite scene:

$$VRP = \sum \phi_{rad} \quad (5)$$

To estimate the TADR, we used the formulation proposed in Coppola et al. (2013):

$$TADR = \frac{VRP}{c_{rad}} \quad (6)$$

In equation (6), c_{rad} is the radiant density [J/m^3] which is calculated as:

$$c_{rad} = \frac{6.45 \times 10^{25}}{X_{SiO2}{}^{10.4}} \quad (7)$$

Where, X_{SiO2} is the silica content of the erupted lava in units of weight percent (wt%). Based on information reported in Coppola et al., (2013), for c_{rad} an uncertainty of ± 50% needs to be considered during the estimates of TADR. Therefore, we calculated the mean TADR from the maximum and minimum value, retrieved from $c_{rad,min}(c_{rad} \times 0.5)$ and $c_{rad,max}$ $(c_{rad} \times 1.5)$ respectively.

4. Results

In this section, we show the results of the Mauna Loa eruption onset investigated through GOES-R ABI data at high temporal resolution. S2-MSI, L8-OLI and L9-OLI2 data (the list of analysed data is reported in Table 3) were used to analyse the active lava flows from fissure vents located on the Northeast Rift Zone, starting from thermal anomalies automatically detected by the NHI system (Marchese & Genzano 2023). The latter provides information about volcanic thermal features over the previous 48 h (https://sites.google.com/view/nhi-tool/home-page), with the advantages of the combined Landsat 8/9 and Sentinel-2 observations (global median average revisit interval of 2.3 days; Li & Chen, 2020).

Table 3
Lava flow area (km^2) and lava flow length (km) (fissure 3) retrieved from S2-MSI, L8-OLI and L9-OLI2 data starting from the NHI detections. N/A (not available) indicates the scene for which the computation of the lava flow length was not performed because of clouds.

Date	Lava flow area (km^2)	Lava flow length (km)
2022/11/28	14.5	4.5
2022/12/01	12.5	15.7
2022/12/02	12.3	16.5
2022/12/03	10.0	16.9
2022/12/06	7.6	N/A
2022/12/08	3.1	5.4
2022/12/10	0.4	2.8

4.1. Mauna Loa eruption onset

Fig. 2a displays the temporal trend of the NHI_{SWIR} retrieved, from GOES-R ABI data of October – December 2022, over the Moku'āweoweo caldera (see pixel marked in purple in Fig. 4). The time series, which does not include the night-time SWIR scenes affected by the sensor background noise recorded in absence of a hot source (e.g., Elvidge et al., 2013), shows that the NHI_{SWIR} was always negative over the summit caldera until the late evening of 27 November 2022.

Indeed, on 28 November at 09:20 UTC (27 November at 23:20 LT), a significant increment of the SWIR signal above the noise level was for the first time recorded, leading to positive values of the used index ($NHI_{SWIR} = 0.27$). Those values indicated the presence of a thermal anomaly at the summit caldera, which was corroborated by the analysis of the GOES-R ABI Level 1b radiance data (1 km spatial resolution). This is indicated by the "bright" pixels, magnified at the top right side of Fig. 3, affecting the Mauna Loa at 09:20 UTC.

Fig. 2b displays a 3-day time series of the NHI_{SWIR} over the period 26–28 November, marked by the red rectangle in Fig. 2a. The plot shows that the index was mostly positive at the caldera since 28 November 2022 at 09:20 UTC, reaching the maximum value of the time series ($NHI_{SWIR} = 0.87$) a few hours later the first detection, when the number of hot pixels also increased.

This is shown in Fig. 4, displaying the ABI CMI band 6 (SWIR2) images of 28 November at 12:00 UTC (left panel) and 12:10 UTC (right panel). Hence, a possible increase in the lava effusion occurred after the 09:27 UTC (01:27 LT), when the lava overflowed the caldera walls (Global Volcanism Program, 2022a). Since 16:30 UTC (06:30 LT), i.e. in concomitance with the HVO overflight confirming the migration of the eruptive activity from the summit to the Northeast Rift Zone, the NHI_{SWIR} progressively decreased, and a few hours later (apart from a new increment ascribable to possible lava cooling effects at the summit caldera) values of the index lower than −0.2 were recorded, until the end of eruption (see Fig. 2a).

Therefore, based on information retrieved from the ABI CMI products, the Mauna Loa eruption started on 28 November 2022, in between 09:10–09:20 UTC (27 November 23:10–23:20 LT). Despite the impact of clouds/plumes on thermal anomaly identification (see Falconieri et al., 2022), the short-term fluctuations of the NHI_{SWIR} marked the increasing/decreasing trends in the lava effusion at the summit caldera, confirming the potential of the index in providing information about high-temperature features also by means of satellite data at high-temporal/low spatial resolution.

4.2. Lava flows mapping

Fig. 5 shows the NHI detections of 28 November – 11 December

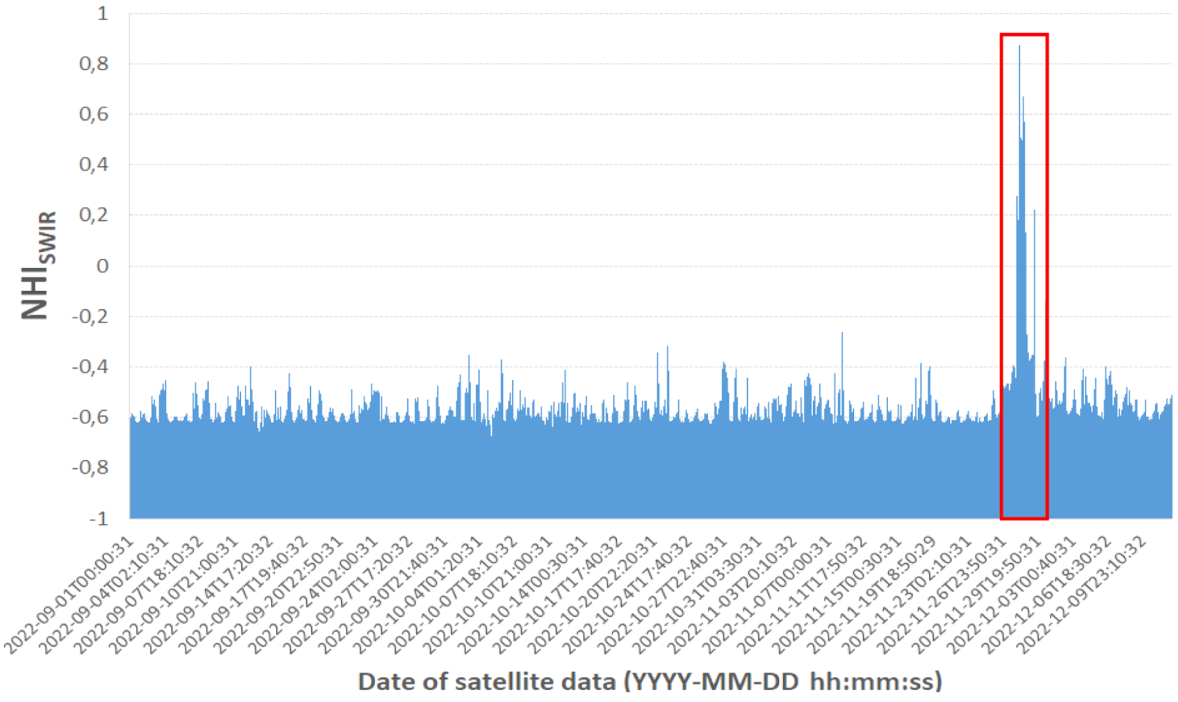

(a)

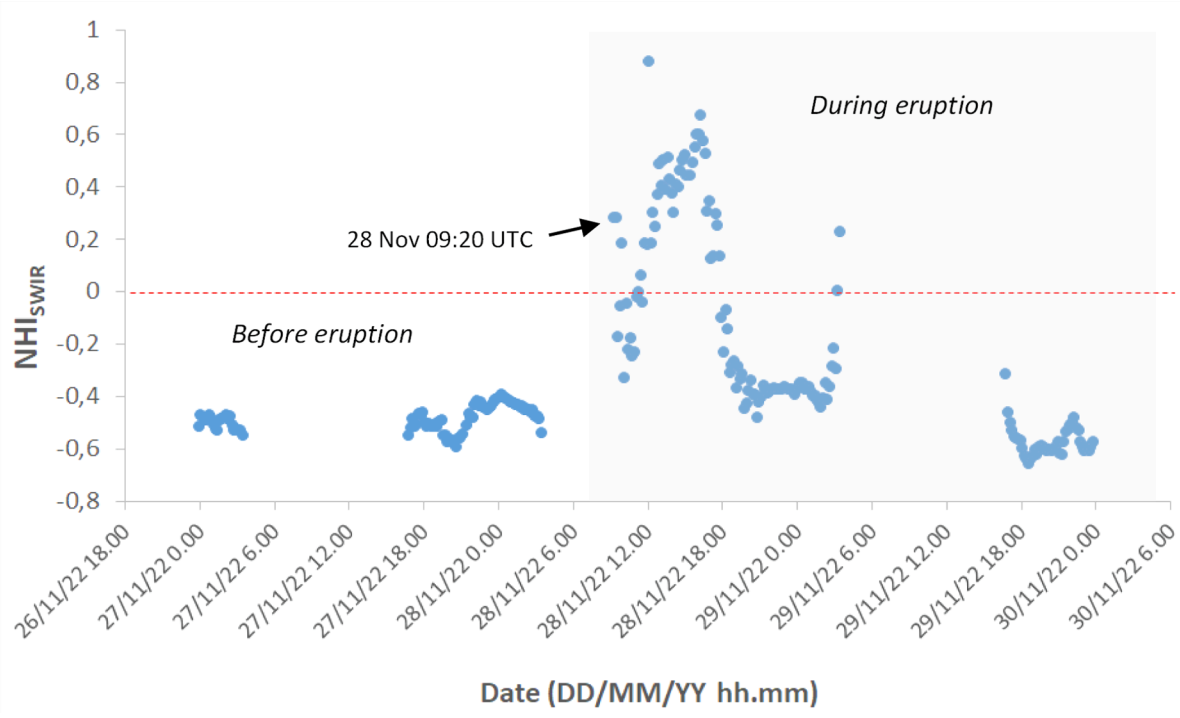

(b)

Fig. 2. A) time series of the NHI_{SWIR} retrieved, from the GOES-R ABI Cloud Moisture Imagery (CMI) products of November-December 2022 over the pixel marked in purple in Fig. 4; b) Time series of the NHI_{SWIR} over the period 26–28 November 2022, marked by the red rectangle in the top panel, with the indication of the time of eruption onset (black arrow) from results of this study. The gaps in data series were due to the sensor background noise, which did not enable a proper computation of the NHI_{SWIR} index in night-time conditions.

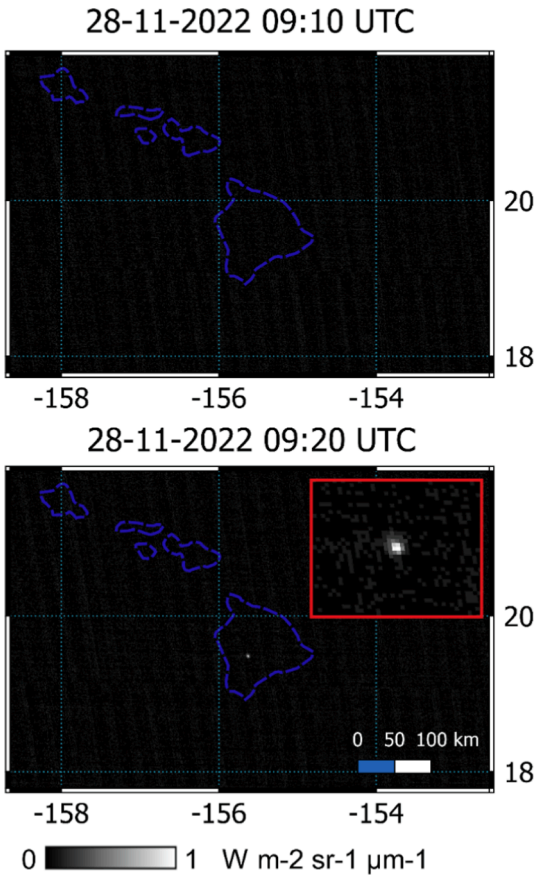

Fig. 3. GOES-R ABI Level 1b radiance data of 28 November at 09:10 UTC (top panel) and 09:20 UTC (bottom panel) acquired in the SWIR1 band (1 km spatial resolution). On the top of bottom panel, the zoom of bright pixels indicating the presence of a thermal anomaly at Mauna Loa, and corroborating the information from the NHI_{SWIR} in Fig. 2.

2022 overlapped on the relief map of the Mauna Loa volcano. The maps display the hot pixels in three different colours, based on their relative intensity level. The NHI system flagged the first thermal anomaly at Mauna Loa on 28 November 2022, from S2-MSI scene of 20:59 UTC (10:59 LT). The latter was acquired about twelve hours after the eruption onset, inferred from the ABI-CMI products (see previous section).

The panel of 28 November displays the lava flows, emitted from the line of fissure vents erupting above 3,048 m (10,000 ft.) elevation on the Northeast Rift Zone, and mapped by NHI. In more detail, the thermal anomaly map indicates that in the morning of 28 November the lava affected the area located in between 12,500–11,000 feet elevation (~3,810–3,350 m). However, while the yellow ($NHI_{SWNIR} > 0$) and violet pixels (i.e., the extremely hot ones; Genzano et al., 2020) were associated with the lava, those depicted in red ($NHI_{SWIR} > 0$) represented artefacts, ascribable to possible blurring effects because of clouds (e.g. Massimetti et al. 2020), as indicated by the analysis of the false colour imagery made available by the NHI system/tool, which is not shown here. On 1 December, the lava flows were observed at the edge of the S2-MSI scene, revealing also some possible smearing effects (e.g., Bignami et al., 2020), which increased the number of red pixels at the borders of the main flow. Despite these issues, the lava flow front was mapped by satellite, at about 6,900 feet elevation (~2,100 m). The L9-OLI2 scene of 2 December enabled a more effective identification of the lava flows from fissure 3, and the thinner flows from the less active fissure 4, also thanks to the cloud-free conditions. The S2-MSI scene of 3 December at 20:59 UTC was affected by clouds, leading to a partial identification of the lava flow areas.

Three days later, the impact of clouds on thermal anomaly identification was even more significant, obscuring most of the main flow. On 8 December, the NHI system mapped the lava flow in between 11,700–9,900 feet elevation (3,535–2,990 m), while it considered inactive the thinner flows below 10,000 feet elevation. On 10 December, the lava flow, affecting the area in between 11,700–10,000 feet elevation, appeared smaller and less intense, as indicated by the few clusters of yellow pixels shown in Fig. 5. The day after, thermal anomaly detected by satellite was entirely ascribable to the lava cooling. Indeed, the Mauna Loa activity declined in between 7 and 9 December and ceased on 10 December; only some incandescence from fissure 3 was observed in the following days(U.S. Geological Survey, 2022l; Global Volcanism Program, 2022b).

The NHI maps of Fig. 5 were consistent with the independent lava flow maps from USGS (https://www.usgs.gov/volcanoes/mauna-loa/maps) especially when clouds and other factors (e.g., data artefacts) did not affect the target area. It is worth mentioning that some USGS maps provided information also about the lava flow length and the total lava flow area. Both parameters were retrieved, in this study, starting from the automated NHI detections, as shown in Table 3.

The latter displays the lava flow area (first column), calculated by the number of hot pixels and the pixel area, and the lava flow length (second

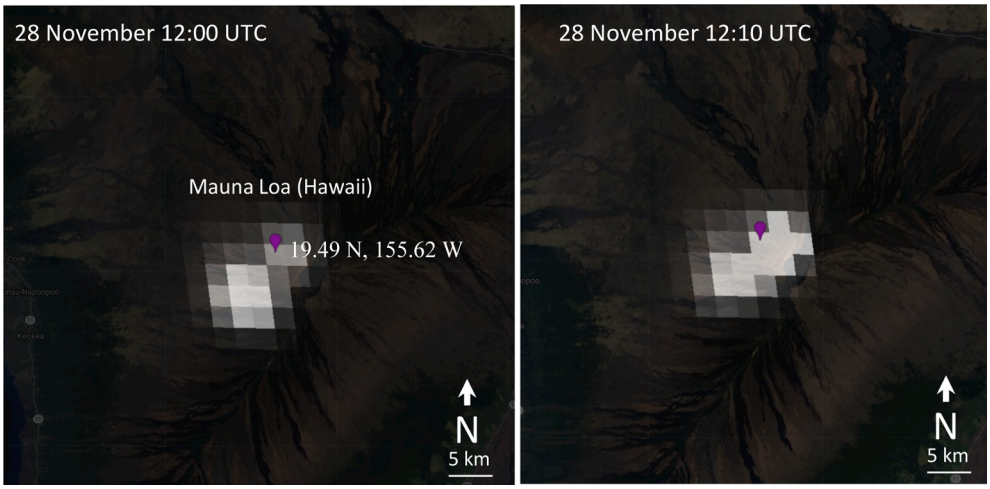

Fig. 4. ABI CMI band 6 (SWIR2) images of 28 November at 12:00 UTC (left panel) and 12:10 UTC (right panel), with indication of the Mauna Loa pixel (19.49 N 155.62 W) analysed in Fig. 2. Brighter tones indicate higher SWIR2 signals. Note the increase of the bright pixels at 12:10 UTC (27 November at 02:10 LT) on the North-East side of the caldera, suggesting a possible increase in the lava effusion, in agreement with the information inferred from Fig. 2.

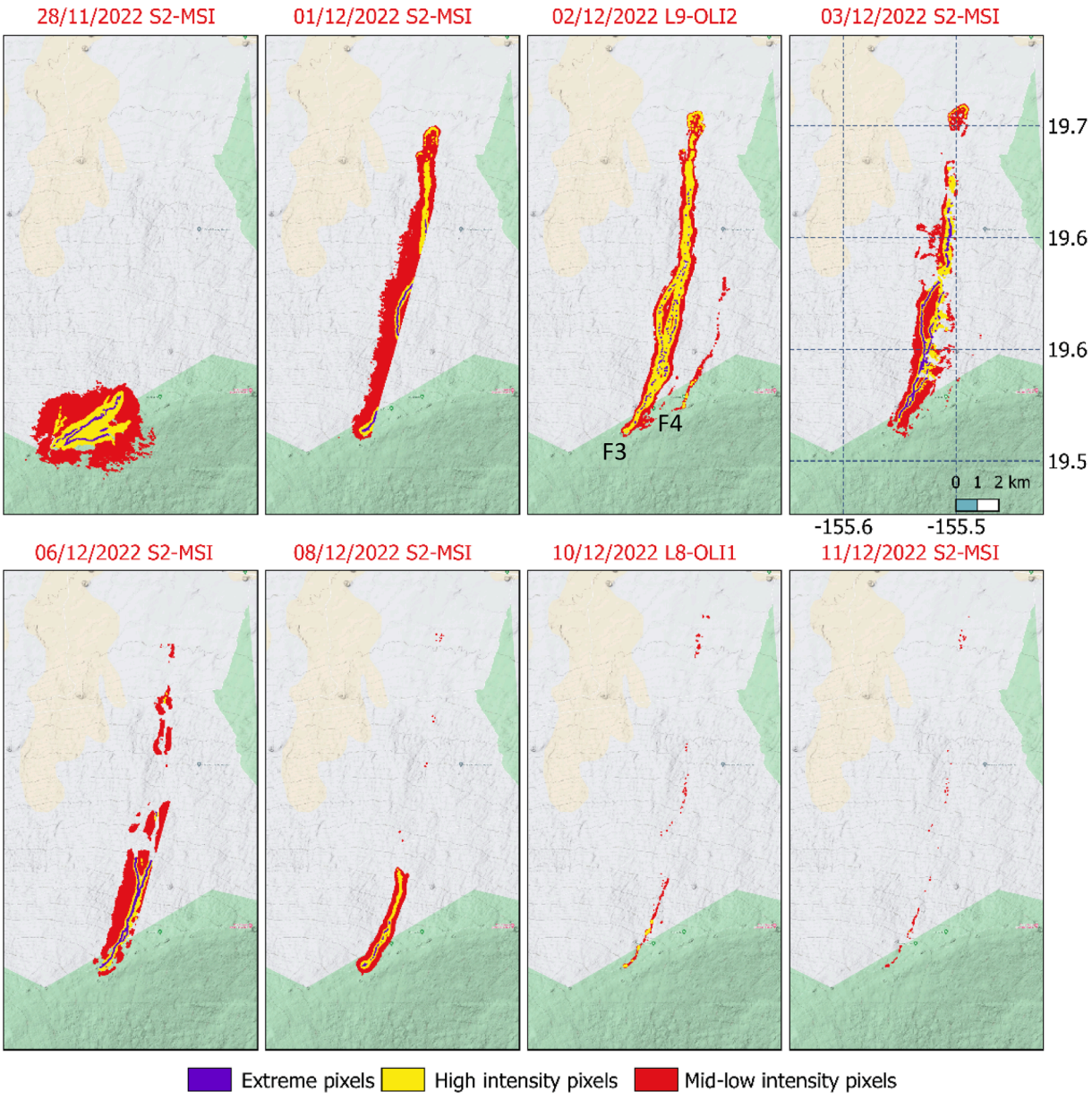

Fig. 5. NHI maps of 28 November (S2-MSI at 20:59 UTC), 1 December (S2-MSI at 21:09 UTC), 2 December (L9-OLI2 at 20:48 UTC), 3 December (S2-MSI at 20:59 UTC), 8 December (S2-MSI at 20:59 UTC), 10 December 2022 (L8-OLI at 20:48 UTC) and 11 December (S2-MSI at 21:09 UTC). Map display the hot pixels in three different colours, based on their different intensity level (see Genzano et al., 2020), and the F3 and F4 fissures.

column). The maximum lava flow area (~14.5 km^2) was estimated on 28 November, in presence of some evident data artefacts leading to an erroneous increase of the hot pixel number (see Fig. 5). On 1 December, the lava flow was observed at the edge of the scene; consequently, the area inundated by the lava was underestimated. Hence also considering the impact of clouds on thermal anomaly identification, the NHI tool provided more accurate information about the lava flow area from satellite scene of 2 December. Regarding the lava flow length (fissure 3), by analysing the S2-MSI, L8-OLI and L9-OLI2 data, we estimated a maximum value of this parameter around 17 km on 3 December, when the lava flow front was still mapped by satellite despite the cloud coverage. Moreover, by analysing the lava flow front in three consecutive satellite scenes, we found that the lava flow from fissure 3 advanced with a speed of ~33 m/hour in between 1 and 2 December, and of ~14 m/hour in between 2 and 3 December. This information agrees with the USGS report of 3 December, according to the lava flow advanced at an average rate of about 13 m per hour over the past 48 h (U.S. Geological Survey, 2022g).

5. Discussion

Previous studies analysed the volcanic eruptions at the early stage generally by means of MIR data, at high temporal resolution, from sensors like SEVIRI (Spinning Enhanced Visible and Infrared Imager), aboard MSG (Meteosat Second Generation) geostationary satellites (e.g., Pergola et al., 2008; Hirn et al., 2009; Ganci et al., 2012). Moreover, only a few works exploited the night-time SWIR observations, mainly in combination with the TIR ones, to characterise the active lava flows (e.g., Hirn et al., 2009). This study shows two main advantages in using SWIR over the MIR data:

- Night-time SWIR observations may provide timely information about effusive eruptions, with a lower dependence on atmospheric effects

and cloudy conditions (e.g., Wooster and Rothery 1997; Elvidge et al., 2013).

- The NHI_{SWIR} index may be used to investigate hot targets, in both daylight and night-time conditions, without performing cloud screening procedures.

Regarding the first point, Fig. 6a displays the time series of the MIR brightness temperature (BT_{MIR}) measured over the ABI pixel previously analysed through the NHI_{SWIR}. The plot shows that the BT_{MIR} was particularly low over the Mauna Loa caldera at the time of eruption onset, due to the presence of a cloud cover, which strongly affected the Big Island of Hawaii (see Fig. 6b).

Fig. 6b shows the GOES-R ABI Level 1b radiance data of 28 November at 09:10 UTC and09:20 UTC (27 November 23:10 LT and23:20 LT) in the MIR band. It is worth noting that while the SWIR imagery revealed the presence of a thermal anomaly at the Mauna Loa since 09:20 UTC (see "bright" pixels in Fig. 2), the same feature was obscured by clouds in the MIR band (BT_{MIR} 255 K at the analysed pixel), where it appeared detectable twenty minutes later (BT_{MIR} 324 K).

This analysis shows that night-time SWIR observations, at high-temporal/coarse spatial resolution, may give a relevant contribution to the early identification and tracking of active lava flows. Concerning the second point, Fig. 2 confirms the different behaviour of the NHI_{SWIR} in presence of hot targets, which favours the discrimination from other features (e.g., meteorological clouds) also when daytime GOES-R ABI data are used (Falconieri et al., 2022).

The NHI_{SWIR} is even more sensitive to the SWIR signal variations when MSI and OLI/OLI2 data, at higher spatial resolution, are used. In this work, the accuracy in the lava flow mapping was affected other than clouds also by data artefacts, associated with blurring/smearing effects (e.g., Bignami et al., 2020; Massimetti et al., 2020; Marchese et al., 2022). These artefacts yielded the overestimation of the lava flow area and mostly affected the NHI_{SWIR} detections, such as lava cooling effects. Therefore, we analysed only the hot pixels flagged by the NHI_{SWNIR}, and the extreme ones of Fig. 5, to characterise the Mauna Loa's lava flows in terms of temperature and volcanic radiative power. This analysis was carried out after correcting daytime SWIR1 data for the influence of the solar-reflected radiation (e.g., Wooster & Kaneko, 2001), using the method discussed in detail Marchese et al., (2022). We did not analyse the S2-MSI scene of 6 December because more affected by clouds.

Fig. 7 compares the total VRP values per satellite acquisition (of S2-MSI and L9-OLI2, calculated over the entire lava flow area mapped by the NHI_{SWNIR}) with the VRP estimates independently retrieved from MODIS and VIIRS. The estimates of VRP were derived from the NASA FIRMS, using the MIR-band approach (see section 1). We selected the MODIS or VIIRS acquisition with the shortest time difference to the corresponding MSI or OLI2 acquisition, respectively. The time gaps between the SWIR and MIR acquisitions vary from 15 min to 3 h 14 min, with a mean time gap of 100 min. SWIR and MIR VRP estimates show the same trend, with SWIR VRP estimates being around 20% higher than the ones from MIR data, which is within the uncertainty range of ±30 % that Wooster et al. (2003) reports for the MIR-band approach. Most of the lava flow area considered for the SWIR VRP estimates (hot pixels flagged by the NHI_{SWNIR}) show T greater than 600 K, i.e., the temperature regime where the MIR-band approach is valid (Wooster et al. 2003). Further, the higher VRP estimates with SWIR data can be explained by the higher spatial resolution of MSI/OLI/OLI2 data, which enables a more detailed and complete identification of the hot pixel area. Moreover, at the time of writing this manuscript, only near real time (NRT) data, and not the final re-processed data of MODIS and VIIRS hotspots, were available at the NASA FIRMS.

The 1 December 2022 acquisition (red dot in Fig. 7) was not considered in the trend analysis, because this S2-MSI imagery covers only $^2/_3$ of the lava flow area (cf. Fig. 5), and therefore underestimates the entire VRP compared to MODIS. Moreover, the MSI scene of 28 November 2022 (VRP = 51024 MW) was also not considered in Fig. 7, as there are no VRP measurements of MODIS or VIIRS within a reasonable time difference (the time gap to the next available MIR VRP is 9 h).

Starting from the total VRP values reported in Table 3 and setting the same average value of the silica content of the 1984 lava samples (X_{SiO2} = 52.3 wt%) (Rhodes, 1984; Harris & Allen, 2008) to derive the c_{rad}, we estimated the TADR through formulation described in section 3.4. By this analysis, we retrieved TADR values up to about 1000 (±500) m^3/s from the L9-OLI2 scene of 2 December 2022. This value and the total erupted volume independently estimated by USGS (Earth Observatory, 2023) seem to indicate that the Mauna Loa eruption of November – December 2022 was comparable, for both intensity and magnitude, to the previous one occurring in March – April 1984. The latter was characterised by a maximum effusion rate above 800 m^3/s recorded prior the 2,900 m vent activity, and by a total erupted volume of 220 × 10^6 m^3 (Lipman & Banks 1987, Rowland et al., 2005).

6. Conclusions

On 27 November 2022, the Mauna Loa Volcano erupted after about 38 years of quiescence. The analysis of GOES-R ABI data, performed through the NHI_{SWIR} time series, indicates that the effusive eruption started on 28 November in between 09:10–09:20 UTC (27 November 23:10–23:20 LT), slightly backdating the eruption onset in comparison with independent information from USGS so far available. Moreover, the short-term variations of the index recorded at the Moku'āweoweo caldera provide information about the increasing/decreasing trend in the lava effusion, occurring before the eruption migration from the summit to the Northeast Rift Zone. The second phase of the Mauna Loa 2022 eruption was investigated starting from the automated NHI detections.

Information about the lava flows emitted from the fissure vents located on the Northeast Rift Zone, retrieved from Sentinel-2 MSI, Landsat 8-OLI and Landsat 9-OLI2 data at mid-high spatial resolution, was consistent with independent maps and reports from USGS, especially in absence of clouds, degassing plumes and data artefacts. By analysing those data, we estimated both the volcanic radiative power (up to 64.8 GW from L9-OLI2 data of 2 December) and the time-averaged discharge rate. The latter indicates that the 2022 eruption of Mauna Loa was comparable, in terms of intensity, to the previous one occurring in 1984.

This study shows that SWIR observations, at different spatial and temporal resolution, may provide a relevant contribution to the monitoring, mapping, and characterisation of volcanic thermal features. Those satellite observations may integrate information derived from MIR and TIR data, which are more suited to identify subtle thermal anomalies (e.g., Girona et al., 2021).

In this direction, a more extensive usage of SWIR data from the ABI sensor is suggested. This could be performed by developing a specific GEE-App capable of supporting the monitoring of active volcanoes covered by the GOES-R satellites by means of the normalised hotspot indices used in this work.

CRediT authorship contribution statement

Nicola Genzano: Software, Formal analysis, Investigation, Writing – original draft, Writing – review & editing. **Francesco Marchese:** Conceptualization, Formal analysis, Investigation, Writing – original draft, Writing – review & editing. **Simon Plank:** Formal analysis, Investigation, Writing – original draft, Writing – review & editing. **Nicola Pergola:** Writing – review & editing, Funding acquisition.

Declaration of Competing Interest

The authors declare that they have no known competing financial interests or personal relationships that could have appeared to influence the work reported in this paper.

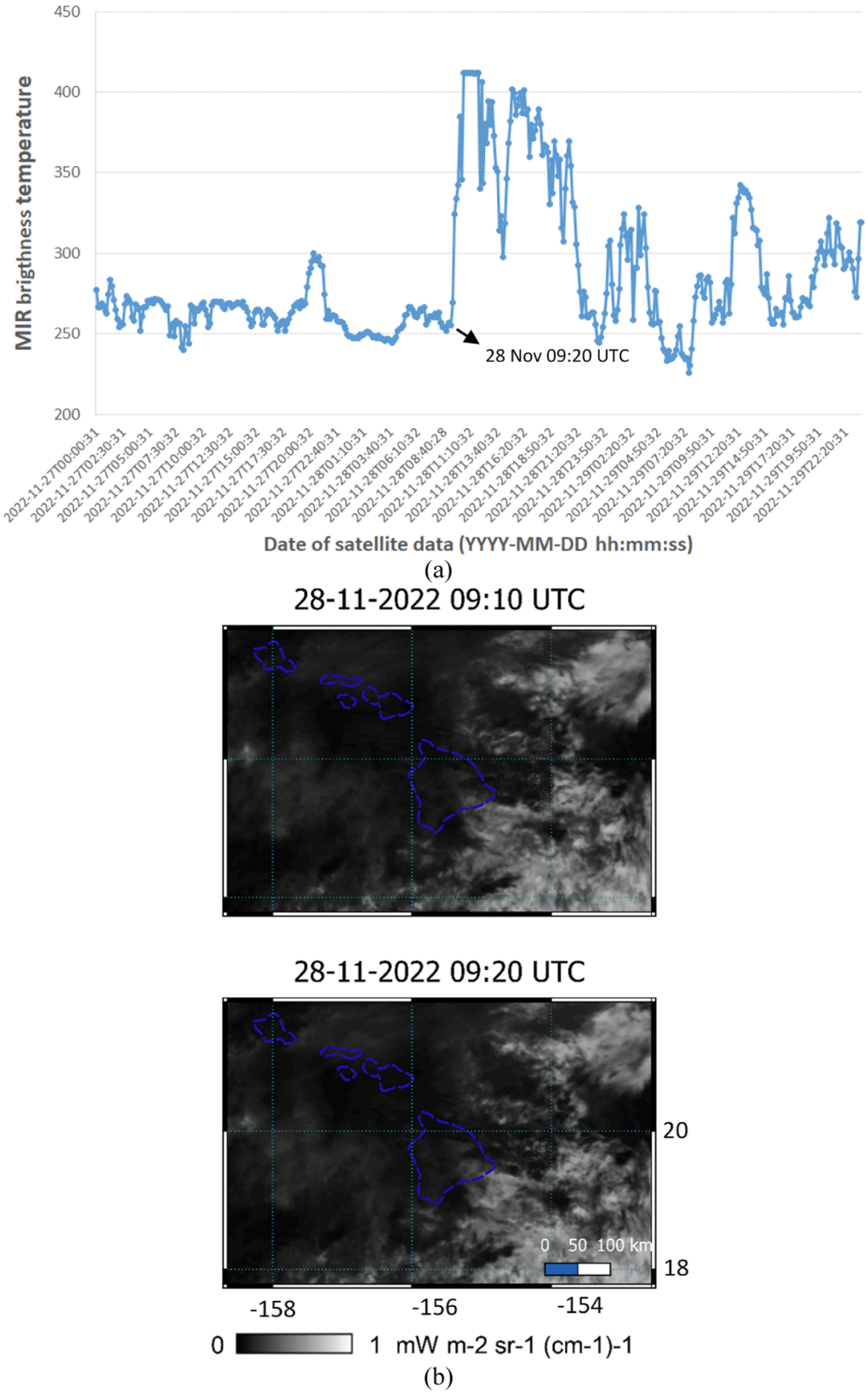

Fig. 6. a) Time series, at 10 min time interval, of the BT_{MIR} retrieved from the ABI CMI products of 26–28 November 2022 over the same caldera pixel of Fig. 3, with indication of the MIR brightness temperature measured on 28 November at 09:20 UTC; b) GOES-R ABI Level 1b radiance data of 28 November at 09:10 UTC (top panels) and 09:20 UTC (bottom panels) acquired in the MIR (2 km spatial resolution) bands.

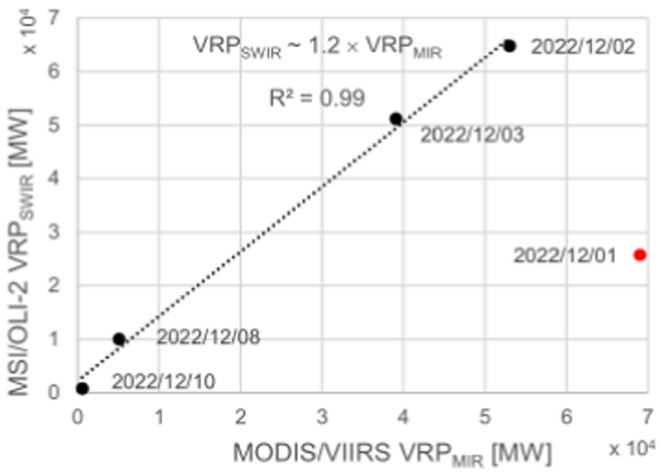

Fig. 7. Correlation plot between VRP-FIRMS (VRP-MIR) and VRP-NHI (VRP-SWIR). Note that the VRP estimates from SWIR (MSI and OLI-2) data are about 20% higher than the VRP estimates from MIR (MODIS and VIIRS) data. Both SWIR and MIR VRP estimates show the same trend. The acquisition of 1 December (red dot) is not considered in the trend analysis, as this S2-MSI scene covers less than $^{2}/_{3}$ of the lava flow and there underestimates the VRP (cf. Fig. 5).

Data availability

The S2-MSI, L8-OLI and L9-OLI2 data analysed in this study were provided by the NHI system/tool, available at https://sites.google.com/view/nhi-tool/home-page. The GOES-R ABI CMI products are available in GEE (Google Earth Engine Platform). The GOES-R ABI radiance data were accessed through the portal https://home.chpc.utah.edu/~u0553130/Brian_Blaylock/cgi-bin/goes16_download.cgi.

Acknowledgments

The USGS photograph and maps (public domain) were used with the permission of the Hawaiian Volcano Observatory, United States Geological Survey (USGS). Nicola Genzano thanks the MUR PON R&I 2014-2020 Program FSE-REACT EU.

References

Amelung, F., Yun, S.H., Walter, T.R., Segall, P., Kim, S.W., 2007. Stress control of deep rift intrusion at Mauna Loa Volcano, Ha-waii. Science 316 (5827), 1026–1030.

Bignami, C., Chini, M., Amici, S., Trasatti, E., 2020. Synergic Use of multi-sensor satellite data for volcanic hazards monitoring: The Fogo (Cape Verde) 2014–2015 effusive eruption. Front. Earth Sci. 8, 22.

Calvari, S., Bonaccorso, A., Ganci, G., 2021. Anatomy of a Paroxysmal Lava Fountain at Etna Volcano: The case of the 12 March 2021, Episode. Rem. Sens. 13 (15), 3052.

Coppola, D., Laiolo, M., Piscopo, D., Cigolini, C., 2013. Rheological control on the radiant density of active lava flows and domes. J. Volcanol. Geotherm. Res. 249, 39–48.

Coppola, D., Laiolo, M., Cigolini, C., Donne, D.D., Ripepe, M., 2016. Enhanced volcanic hot-spot detection using MODIS IR data: results from the MIROVA system. Geol. Soc. London Special Publicat. 426 (1), 181–205.

Coppola, D., Laiolo, M., Cigolini, C., Massimetti, F., Delle Donne, D., Ripepe, M., et al., 2020. Thermal remote sensing for global volcano monitoring: experiences from the MIROVA system. Front. Earth Sci. 7, 362.

Dozier, J., 1981. A method for satellite identification of surface temperature fields of subpixel resolution. Rem. Sens. Environ. 11, 221–229.

Earth Engine Data Catalogue, 2022. GOES-16 MCMIPM Series ABI Level 2 Cloud and Moisture Imagery Mesoscale. https://developers.google.com/earth-engine/datasets/catalog/NOAA_GOES_16_MCMIPM Accessed 13 December 2022.

Earth Observatory, 2023. Sizing up Mauna Loa's Lava Flows https://earthobservatory.nasa.gov/images/150736/sizing-up-mauna-loas-lava-flows Accessed 2 February 2022.

Elvidge, C.D., Zhizhin, M., Hsu, F.C., Baugh, K.E., 2013. VIIRS nightfire: Satellite pyrometry at night. Remote Sens. 5 (9), 4423–4449.

European Space Agency, 2022. "Sentinel Online. Resolution and Swath, Spatial and Spectral Resolutions." https://sentinels.copernicus.eu/web/sentinel/missions/sentinel-2/instrument-payload/resolution-and-swath Accessed 13 December 2022.

Falconieri, A., Genzano, N., Mazzeo, G., Pergola, N., Marchese, F., 2022. First Implementation of a normalized hotspot index on Himawari-8 and GOES-R data for the active volcanoes monitoring: results and future developments. Remote Sens. 14 (21).

Faruolo, M., Falconieri, A., Genzano, N., Lacava, T., Marchese, F., Pergola, N., 2022a. A daytime multisensor satellite system for global gas flaring monitoring. IEEE Trans. Geosci. Remote Sens. 60, 1–17.

Faruolo, M., Genzano, N., Marchese, F., Pergola, N., 2022b. A Tailored approach for the global gas flaring investigation by means of daytime satellite imagery. Remote Sens. 14 (24), 6319.

Ganci, G., Vicari, A., Cappello, A., Del Negro, C., 2012. An emergent strategy for volcano hazard assessment: From thermal satellite monitoring to lava flow modeling. Remote Sens. Environ. 119, 197–207.

Ganci, G., Cappello, A., Bilotta, G., Del Negro, C., 2020. How the variety of satellite remote sensing data over volcanoes can assist hazard monitoring efforts: The 2011 eruption of Nabro volcano. Remote Sens. Environ. 236, 111426.

Genzano, N., Pergola, N., Marchese, F., 2020. A Google Earth Engine tool to investigate, map and monitor volcanic thermal anomalies at global scale by means of mid-high spatial resolution satellite data. Remote Sens. 12 (19), 3232.

Girona, T., Realmuto, V., Lundgren, P., 2021. Large-scale thermal unrest of volcanoes for years prior to eruption. Nature Geoscience 14 (4), 238–241.

Global Volcanism Program, 2012. Report on Mauna Loa (United States) (Dennen, R., and Wunderman, R., eds.). Bulletin of the Global Volcanism Network, 2012, 37:5. Smithsonian Institution. Doi: 10.5479/si.GVP.BGVN201205-332020 Accessed 5 December 2022.

Global Volcanism Program, 2022a. Report on Mauna Loa (United States). In: Sennert, S K (Ed.), Weekly Volcanic Activity Report, 7 December-13 December 2022. Smithsonian Institution and US Geological Survey.

Global Volcanism Program, 2022b. Report on Mauna Loa (United States). In: Sennert, S K (Ed.), Weekly Volcanic Activity Report, 5 October-11 October 2022. Smithsonian Institution and US Geological Survey.

Gorelick, N., Hancher, M., Dixon, M., Ilyushchenko, S., Thau, D., Moore, R., 2017. Google earth engine: Planetary-scale geospatial analysis for everyone. Remote Sens. Environ. 202, 18–27.

Gray, D.M., Burton-Johnson, A., Fretwell, P.T., 2019. Evidence for a lava lake on Mt. Michael volcano, Saunders Island (South Sandwich Islands) from Landsat, Sentinel-2 and ASTER satellite imagery. J. Volcanol. Geotherm. Res. 379, 60–71.

Gunshor, M., Schmit, T.J., Pogorzala, D.R., Lindstrom, S.S., Nelson, J.P., 2020. GOES-R series ABI imagery artifacts. J. Appl. Remote Sens. 14 (3), 032411.

Harris, A.J., Allen III, J.S., 2008. One-, two-and three-phase viscosity treatments for basaltic lava flows. J. Geophys. Res.: Solid Earth 113 (B9).

Harris, A.J., Flynn, L.P., Rothery, D.A., Oppenheimer, C., Sherman, S.B., 1999. Mass flux measurements at active lava lakes: implications for magma recycling. J. Geophys. Res.: Solid Earth 104 (B4), 7117–7136.

Harris, A.J., Dehn, J., Calvari, S., 2007. Lava effusion rate definition and measurement: a review. Bull. Volcanol. 70 (1), 1–22.

Harris, A.J.L., Pilger, E., Flynn, L.P., Garbeil, H., Mouginis-Mark, P.J., Kauahikaua, J., Thornber, C., 2001. Automated, high temporal resolution, thermal analysis of Kilauea volcano, Hawai'i, using GOES satellite data. Int. J. Remote Sens. 22 (6), 945–967.

Higgins, J., Harris, A., 1997. VAST: A program to locate and analyse volcanic thermal anomalies automatically from remotely sensed data. Comput. Geosci. 23 (6), 627–645.

Hirn, B., Di Bartola, C., Ferrucci, F., 2009. Combined use of SEVIRI and MODIS for detecting, measuring, and monitoring active lava flows at erupting volcanoes. IEEE Trans. Geosci. Remote Sens. 47 (8), 2923–2930.

Kato, S., Miyamoto, H., Amici, S., Oda, A., Matsushita, H., Nakamura, R., 2021. Automated classification of heat sources detected using SWIR remote sensing. Int. J. Appl. Earth Observ. Geoinform. 103, 102491.

Li, J., Chen, B., 2020. Global revisit interval analysis of Landsat-8-9 and Sentinel-2A-2B data for terrestrial monitoring. Sensors 20 (22), 6631.

Lipman, P.W., Banks, N.G., 1987. AA flow dynamics, Mauna Loa 1984. U.S. Geol. Survey Prof Pap 1350, 1527–1567.

Lipman, P.W., Banks, N.G., Rhodes, J.M., 1985. Degassing-induced crystallization of basaltic magma and effects on lava rheology. Nature 317 (6038), 604–607.

Lockwood, J., Banks, N., English, T., Greenland, P., Jackson, D., Johnson, D., et al., 1985. The 1984 eruption of Mauna Loa Volcano, Hawaii. Eos, Transact. Am. Geophys. Union 66 (16), 169–171.

Lombardo, V., Pick, L., Spinetti, C., Tadeucci, J., Zakšek, K., 2020. Temperature and emissivity separation 'draping' algorithm applied to hyperspectral infrared data. Rem. Sens. 12, 2046.

Marchese, F., Genzano, N., Nolde, M., Falconieri, A., Pergola, N., Plank, S., 2022. Mapping and characterizing the Kilauea (Hawai'i) lava lake through Sentinel-2 MSI and Landsat-8 OLI observations of December 2020–February 2021. Environ. Model. Software 148, 105273.

Marchese, F., Genzano, N., 2023. Global volcano monitoring through the Normalized Hotspot Indices (NHI) system. J. Geol. Soc. 180 (1) jgs2022-014.

Marchese, F., Lacava, T., Pergola, N., Hattori, K., Miraglia, E., Tramutoli, V., 2012. Inferring phases of thermal unrest at Mt. Asama (Japan) from infrared satellite observations. J. Volcanol. Geotherm. Res. 237, 10–18.

Marchese, F., Neri, M., Falconieri, A., Lacava, T., Mazzeo, G., Pergola, N., Tramutoli, V., 2018. The contribution of multi-sensor infrared satellite observations to monitor Mt. Etna (Italy) activity during May to August 2016. Remote Sens. 10 (12), 1948.

Marchese, F., Genzano, N., Neri, M., Falconieri, A., Mazzeo, G., Pergola, N., 2019. A multi-channel algorithm for mapping volcanic thermal anomalies by means of Sentinel-2 MSI and Landsat-8 OLI Data. Remote Sens. 11, 2876.

Massimetti, F., Coppola, D., Laiolo, M., Valade, S., Cigolini, C., Ripepe, M., 2020. Volcanic hot-spot detection using SENTINEL-2: a comparison with MODIS–MIROVA thermal data series. Remote Sens. 12 (5), 820.
Miklius, A., Cervelli, P., 2003. Interaction between Kilauea and Mauna Loa. Nature 421 (229).
Mouginis-Mark, P., Snell, H., Ellisor, R., 2000. GOES satellite and field observations of the 1998 eruption of Volcan Cerro Azul, Galápagos Islands. Bull. Volcanol. 62, 188–198.
Murphy, S.W., Wright, R., Oppenheimer, C., de Souza Filho, C.R., 2013. MODIS and ASTER synergy for characterizing thermal volcanic activity. Remote Sens. Environ. 131, 195–205.
Murphy, S.W., de Souza Filho, C.R., Wright, R., Sabatino, R., Pabon, C., 2016. HOTMAP: Global hot target detection at moderate spatial resolution. Remote Sens. Environ. 177, 78–88.
Musacchio, M., Silvestri, M., Rabuffi, F., Buongiorno, M.F., Falcone, S., 2023. Kīlauea-Leilani 2018 lava flow delineation using Sentinel2 and Landsat8 images. Geol. Soc. London, Special Publicat. 519 (1), SP519-2020.
National Aeronautics and Space Administration, 2022. Landsat-9 Instruments. https://landsat.gsfc.nasa.gov/satellites/landsat-9/landsat-9-instruments/ Accessed 15 December 2022.
National Oceanic and Atmospheric Administration (NOAA)—National Environmental Satellite, Data, and Information Service, 2012 (NESDIS). "Theoretical Basis Document for Cloud and Moisture Imagery Product (CMIP)". https://www.star.nesdis.noaa.gov/goesr/documents/ATBDs/Baseline/ATBD_GOES-R_ABI_CMI_KPP_v3.0_July2012.pdf Accessed on 6 September 2022.
Orynbaikyzy, A., Plank, S., Vetrita, Y., Martinis, S., Santoso, I., Ismanto, R.D., et al., 2023. Joint use of Sentinel-2 and Sentinel-1 data for rapid mapping of volcanic eruption deposits in Southeast Asia. Int. J. Appl. Earth Observ. Geoinform. 116, 103166.
Pergola, N., Marchese, F., Tramutoli, V., 2004. Automated detection of thermal features of active volcanoes by means of infrared AVHRR records. Remote Sens. Environ. 93 (3), 311–327.
Pergola, N., Marchese, F., Tramutoli, V., Filizzola, C., Ciampa, M., 2008. Advanced satellite technique for volcanic activity monitoring and early warning. Ann. Geophys. 1 (51), 287–301.
Piscini, A., Lombardo, V., 2014. Volcanic hot spot detection from optical multispectral remote sensing data using artificial neural networks. Geophys. J. Int. 196 (3), 1525–1535.
Plank, S., Marchese, F., Genzano, N., Nolde, M., Martinis, S., 2020. The short life of the volcanic island New Late'iki (Tonga) analyzed by multi-sensor remote sensing data. Sci. Rep. 10 (1), 22293.
Plank, S., Massimetti, F., Soldati, A., Hess, K.U., Nolde, M., Martinis, S., Dingwell, D.B., 2021. Estimates of lava discharge rate of 2018 Kīlauea Volcano, Hawai'i eruption using multi-sensor satellite and laboratory measurements. Int. J. Remote Sens. 42 (4), 1492–1511.
Rhodes, J.M., 1984. Geochemistry of the 1984 Mauna Loa eruption Implications for magma storage and supply. Journal of Geophysical Research 93 (B5), 4453–4466.
Riker, J.M., Cashman, K.V., Kauahikaua, J.P., Montierth, C.M., 2009. The length of channelized lava flows: Insight from the 1859 eruption of Mauna Loa Volcano, Hawaii. J. Volcanol. Geotherm. Res. 183 (3–4), 139–156.
Rösch, M., Plank, S., 2022. Detailed mapping of lava and ash deposits at Indonesian volcanoes by means of VHR PlanetScope change detection. Remote Sens. 14 (5), 1168.
Rowland, S.K., Garbeil, H., Harris, A.J., 2005. Lengths and hazards from channel-fed lava flows on Mauna Loa, Hawai 'i, determined from thermal and downslope modeling with FLOWGO. Bull. Volcanol. 67 (7), 634–647.
Thompson, J.O., Contreras-Arratia, R., Befus, K.S., Ramsey, M.S., 2022. Thermal and seismic precursors to the explosive eruption at La Soufrière Volcano, St. Vincent in April 2021. Earth Planet. Sci. Lett. 592, 117621.
U.S. Geological Survey, 2022a. Mauna Loa, Geology and History. Available online: https://www.usgs.gov/volcanoes/mauna-loa/geology-and-history Accessed 5 December 2022.
U.S. Geological Survey, 2022b. Mauna Loa, Geology and History. March 25 – April 15, 1984 https://www.usgs.gov/volcanoes/mauna-loa/march-25-april-15-1984 Accessed 5 December 2022.
U.S. Geological Survey, 2022c. Hazard Notification System (HANS) for Volcanoes. Hawaiian Volcano Observatory Daily Update. November 27, 2022, 8:38 AM HST (Sunday, November 27, 2022, 18:38 UTC). https://volcanoes.usgs.gov/hans2/view/notice/DOI-USGS-HVO-2022-11-27T10:32:56-08:00 Accessed 5 December 2022.
U.S. Geological Survey, 2022d. "Hazard Notification System (HANS) for Volcanoes. Hawaiian Volcano Observatory Status Report. Tuesday, November 29, 2022, 4:23 PM HST (Wednesday, November 30, 2022, 02:23 UTC). Mauna Loa Volcano (VNUM #332020)." https://volcanoes.usgs.gov/hans2/view/notice/DOI-USGS-HVO-2022-11-29T18:12:13-08:00 Accessed 5 December 2022.
U.S. Geological Survey, 2022e. Hazard Notification System (HANS) for Volcanoes. Hawaiian Volcano Observatory Status Report. Wednesday, November 30, 2022, 4:10 PM HST (Thursday, December 1, 2022, 02:10 UTC). https://volcanoes.usgs.gov/hans2/view/notice/DOI-USGS-HVO-2022-11-30T18:05:22-08:00 Accessed 5 December 2022.
U.S. Geological Survey, 2022f. Hazard Notification System (HANS) for Volcanoes. "Hawaiian Volcano Observatory Status Report. Friday, December 2, 2022, 4:39 PM HST (Saturday, December 3, 2022, 02:39 UTC). https://volcanoes.usgs.gov/hans2/view/notice/DOI-USGS-HVO-2022-12-02T18:37:23-08:00 Accessed 5 December 2022.
U.S. Geological Survey, 2022g. "Hazard Notification System (HANS) for Volcanoes. Hawaiian Volcano Observatory Daily Update. Saturday, December 3, 2022, 8:45 AM HST (Saturday, December 3, 2022, 18:45 UTC). Mauna Loa Volcano (VNUM #332020) https://volcanoes.usgs.gov/hans2/view/notice/DOI-USGS-HVO-2022-12-03T10:41:11-08:00.
U.S. Geological Survey. 2022h. "Hazard Notification System (HANS) for Volcanoes. Hawaiian Volcano Observatory Daily Update. Monday, December 5, 2022, 9:04 AM HST (Monday, December 5, 2022, 19:04 UTC). Mauna Loa Volcano (VNUM #332020). https://volcanoes.usgs.gov/hans2/view/notice/DOI-USGS-HVO-2022-12-05T10:59:59-08:00) Accessed 6 December 2022.
U.S. Geological Survey 2022i. "Hazard Notification System (HANS) for Volcanoes. Hawaiian Volcano Observatory Status Report. Monday, December 5, 2022, 4:23 PM HST (Tuesday, December 6, 2022, 02:23 UTC). Mauna Loa Volcano (VNUM #332020)." https://volcanoes.usgs.gov/hans2/view/notice/DOI-USGS-HVO-2022-12-05T18:13:21-08:00 Accessed 6 December 2022.
U.S. Geological Survey. 2022l. "Hazard Notification System (HANS) for Volcanoes. HVO/USGS Volcanic Activity Notice (VNUM #332020)." https://volcanoes.usgs.gov/hans2/view/notice/DOI-USGS-HVO-2022-12-13T08:57:10-08:00 Accessed 15 December 2022.
U.S. Geological Survey, 2022m. Mauna Loa Geology and History. November 27-December 10, 2022. Mauna Loa had not erupted since 1984—its longest quiet period in recorded history. https://www.usgs.gov/volcanoes/mauna-loa/november-27-december-10-2022 Accessed 2 May 2023.
Vaughan, R.G., Kervyn, M., Realmuto, V., Abrams, M., Hook, S.J., 2008. Satellite measurements of recent volcanic activity at Oldoinyo Lengai, Tanzania. J. Volcanol. Geotherm. Res. 173 (3–4), 196–206.
Wooster, M.J., Kaneko, T., 2001. Testing the accuracy of solar-reflected radiation corrections applied during satellite shortwave infrared thermal analysis of active volcanoes. J. Geophys. Res.: Solid Earth 106 (B7), 13381–13393.
Wooster, M.J., Rothery, D.A., 1997. Thermal monitoring of Lascar Volcano, Chile, using infrared data from the along-track scanning radiometer: a 1992–1995 time series. Bulletin of Volcanology 58, 566–579.
Wooster, M.J., Zhukov, B., Oertel, D., 2003. Fire radiative energy for quantitative study of biomass burning: Derivation from the BIRD experimental satellite and comparison to MODIS fire products. Remote Sens. Environ. 86 (1), 83–107.
Wright, R., Flynn, L., Garbeil, H., Harris, A., Pilger, E., 2002. Automated volcanic eruption detection using MODIS. Remote Sens. Environ. 82 (1), 135–155.
Wright, R., Pilger, E., 2008. Radiant flux from Earth's subaerially erupting volcanoes. Int. J. Remote Sens. 29 (22), 6443–6466.
Wright, R., Blackett, M., Hill-Butler, C., 2015. Some observations regarding the thermal flux from Earth's erupting volcanoes for the period of 2000 to 2014. Geophys. Res. Lett. 42 (2), 282–289.
Wu, W., Liu, Y., Rogers, B.M., Xu, W., Dong, Y., Lu, W., 2022. Monitoring gas flaring in Texas using time-series sentinel-2 MSI and landsat-8 OLI images. Int. J. Appl. Earth Observ. Geoinform. 114, 103075.
Zhao, Y., Ban, Y., 2022. GOES-R time series for early detection of wildfires with deep GRU-network. Remote Sens. 14 (17), 4347.